Appl. Phys. A 78, 1129–1136 (2004)
DOI: 10.1007/s00339-003-2464-2

Applied Physics A
Materials Science & Processing

C.D. SPATARU[1,2]
S. ISMAIL-BEIGI[1,2]
L.X. BENEDICT[3]
S.G. LOUIE[1,2,✉]

Quasiparticle energies, excitonic effects and optical absorption spectra of small-diameter single-walled carbon nanotubes

[1] Department of Physics, University of California at Berkeley, Berkeley, CA 94720, USA
[2] Materials Sciences Division, Lawrence Berkeley National Laboratory, Berkeley, CA 94720, USA
[3] H Division, Physics and Advanced Technologies Directorate, Lawrence Livermore National Laboratory, University of California, Livermore, CA 94550, USA

Received: 15 October 2003/Accepted: 28 October 2003
Published online: 9 March 2004 •

ABSTRACT We present a first-principles study of the effects of many-electron interactions on the optical properties of single-walled carbon nanotubes. Motivated by recent experiments, we have carried out ab initio calculations on the single-walled carbon nanotubes (3, 3), (5, 0) and (8, 0). The calculations are based on a many-body Green's function approach in which both the quasiparticle (single-particle) excitation spectrum and the optical (electron–hole excitation) spectrum are determined. We show that the optical spectrum of both the semiconducting and metallic nanotubes studied exhibits important excitonic effects due to their quasi-one-dimensional nature. Binding energies for excitonic states range from zero for the metallic (5, 0) tube to nearly 1 eV for the semiconducting (8, 0) tube. Moreover, the metallic (3, 3) tube possesses exciton states bound by nearly 100 meV. Our calculated spectra explain quantitatively the observed features found in the measured spectra.

PACS 78.67.Ch; 71.35.Cc; 73.22.-f

1 Introduction

Recent advances in the measurement of the optical properties of individual single-walled carbon nanotubes (SWCNTs) [1–3] have generated a great deal of interest and provided a wealth of information, but they also have raised questions and highlighted real puzzles in our fundamental understanding of nanotubes. In particular, standard single-particle, interband theories are unable to explain many of the relevant optical measurements. Many-electron interactions have been shown [4] to be of importance in quasi-one-dimensional systems such as nanotubes and can drastically modify the predictions of interband theories. But, the actual effects of these interactions on the optical properties of real nanotubes have not been elucidated to date. We present here state-of-the-art, first-principles calculations of the optical properties of carbon nanotubes with inclusion of the relevant many-electron effects. We show the crucial role played by many-electron interactions in modifying the optical properties of both metallic and semiconducting nanotubes. Once many-electron interactions are included, our findings explain quantitatively existing experimental data. These many-electron effects give rise to new phenomena and can provide a basis for possible applications [5].

✉ E-mail: sglouie@uclink.berkeley.edu

2 Theoretical method

In this study, we compute the optical absorption spectra of the small-diameter SWCNTs (3, 3), (5, 0) and (8, 0). The calculations use a recently developed approach in which electron–hole excitations and optical spectra of real materials are calculated from first principles [6]. The calculations have three stages.

First, we treat the electronic ground state with ab initio pseudopotential density-functional theory (DFT), in which the Kohn–Sham electronic states are given by

$$\left[-\frac{\nabla^2}{2} + V_{\text{ion}} + V_{\text{Hartree}} + V_{\text{xc}}^{\text{LDA}}\right]\psi_{n\boldsymbol{k}} = E_{n\boldsymbol{k}}^{\text{LDA}}\psi_{n\boldsymbol{k}}. \tag{1}$$

For the exchange-correlation potential V_{xc}, we employ the local density approximation (LDA) [7]. The eigenfunctions $\psi_{n\boldsymbol{k}}$ are used in the next stage as very good approximations for the quasiparticle wavefunctions [8].

Second, we obtain the quasiparticle (single-particle excitation) energies $E_{n\boldsymbol{k}}$ by solving the Dyson equation [8]

$$\left[-\frac{\nabla^2}{2} + V_{\text{ion}} + V_{\text{Hartree}} + \Sigma(E_{n\boldsymbol{k}})\right]\psi_{n\boldsymbol{k}} = E_{n\boldsymbol{k}}\psi_{n\boldsymbol{k}}. \tag{2}$$

Here, the self-energy Σ is calculated within the GW approximation [8, 9]

$$\Sigma = \mathrm{i}GW, \tag{3}$$

where G is the one-particle Green's function and W the screened Coulomb interaction calculated using the dielectric screening matrix ε within the random-phase approximation (RPA).

Third, we calculate the coupled electron–hole excitation energies Ω^S and the optical spectrum by solving the Bethe–Salpeter equation [6, 10]

$$(E_{c\boldsymbol{k}} - E_{v\boldsymbol{k}})\,A_{vc\boldsymbol{k}}^S + \sum_{\boldsymbol{k}'v'c'}\langle vc\boldsymbol{k}|K^{\text{eh}}|v'c'\boldsymbol{k}'\rangle A_{v'c'\boldsymbol{k}'}^S = \Omega^S A_{vc\boldsymbol{k}}^S, \tag{4}$$

where $A^S_{vc\boldsymbol{k}}$ is the exciton amplitude in $\boldsymbol{k}$-space, $K^{\rm eh}$ is the electron–hole interaction kernel and $|c\boldsymbol{k}\rangle$ and $|v\boldsymbol{k}\rangle$ are the quasielectron and quasihole states, respectively. $K^{\rm eh}$ has two terms: an attractive direct term involving the screened Coulomb interaction and a repulsive exchange term involving the bare Coulomb interaction [6]. Both terms are calculated from first principles in the present approach.

2.1 *Technical details*

The DFT wavefunctions and eigenvalues are obtained by solving the Kohn–Sham equations in a plane-wave basis with an energy cutoff of 60 Ry. We use ab initio pseudopotentials generated within the scheme of Troullier and Martins [11] combined with the Kleinman–Bylander form [12] to produce a separable potential (we used the p channel as the local part of the pseudopotential and a cutoff radius in real space $r_{\rm c} = 1.4$ a.u.). To mimic the property of individual SWCNTs, we carry out calculations with an array of well-separated nanotubes in a supercell arrangement. The supercell geometry is hexagonal, with the smallest intertube distance being 9.7 Å. The structure of the tubes is determined by relaxing the atomic positions with the intertube distance fixed until the forces on the atoms are all less than 0.01 eV/Å. The diameters of the relaxed tubes are 4.17 Å for the (3, 3) tube, 4.03 Å for the (5, 0) tube and 6.31 Å for the (8, 0) tube. The lattice vector along the tube axis ($\hat{z}$) has lengths 2.43 Å for the armchair tube (3, 3) and 4.21 Å for the zigzag tubes (5, 0) and (8, 0). For the calculations of nanotubes inside channels of zeolites (see below), we use the intertube geometry as dictated by the zeolite crystal structure. A simple tight-binding model would predict the (5, 0) tube to be a semiconductor; however, as we discuss later, this tube is a metal as a consequence of strong curvature effects [13].

The *GW* and Bethe–Salpeter calculations were converged with respect to the number of bands, the energy cutoffs in Σ and $K^{\rm eh}$ and the number of $\boldsymbol{k}$-points used to sample the first Brillouin zone. For the *GW* calculations, we used up to 64 $\boldsymbol{k}$-points and conduction bands within an energy range of 42 eV above the Fermi level. Crystalline local field effects were included up to an energy cutoff of 12 Ry. In the Bethe–Salpeter calculations, we used up to 400 $\boldsymbol{k}$-points and 10 valence and 10 conduction bands, and crystalline local field effects were included up to an energy cutoff of 7 Ry.

2.2 *Truncation of the Coulomb potential in a cylindrical geometry*

In supercell calculations for semiconducting tubes, due to the long-range nature of the screened Coulomb interaction, non-physical interaction between periodic image charges can lead to deviations from the physics of an isolated system. (We find negligible tube–tube interactions or image effects for metallic tubes, where screening is complete.) Therefore, we truncate the Coulomb interaction in a cylindrical geometry for the semiconducting tubes:

$$\hat{v}_{\rm c}(\boldsymbol{r}) = \frac{1}{r}\theta(\varrho - \varrho_{\rm c})\theta(|z| - z_{\rm c}), \tag{5}$$

where $\varrho = \sqrt{x^2 + y^2}$ is the radial coordinate perpendicular to the tube axis ($\hat{z}$). We choose the cutoff $\varrho_{\rm c}$ equal to half the intertube distance d_t (making sure that d_t is large enough). As for the cutoff $z_{\rm c}$ along $\hat{z}$, it has to be larger than the size of the excitons (typically $\sim$ a few tens of Å) in the Bethe–Salpeter calculations and smaller than the effective supercell size along the tube direction (dictated by the number of discretized $\boldsymbol{k}$-points used to sample the Brillouin zone along $\hat{z}$). In momentum space, the expression for the truncated Coulomb potential reads:

$$\hat{v}_{\rm c}(\boldsymbol{q}) = 4\pi \int_0^{\varrho_{\rm c}} {\rm d}s\, sJ_0(q_{xy}s) \int_0^{z_{\rm c}} {\rm d}t \frac{\cos(q_z t)}{\sqrt{s^2 + t^2}}, \tag{6}$$

where $q_{xy} = \sqrt{q_x^2 + q_y^2}$.

With sufficiently large cutoffs, the use of truncation rids us of the non-physical interaction between periodic image charges and has a further advantage: there is no need to sample the Brillouin zone in directions perpendicular to $\hat{z}$. Thus, throughout our calculations, we use a $1 \times 1 \times n$ Monkhorst–Pack mesh for the $\boldsymbol{k}$-point sampling. There is however a price to be paid: n is generally larger in the truncated case than in the untruncated case. This is exemplified in Fig. 1 which shows the head element ε^{-1}_{00} of the static inverse dielectric matrix for the semiconducting tube (8, 0). In the truncated case, ε^{-1}_{00} as a function of q_z has a sharper profile near $q_z = 0$.

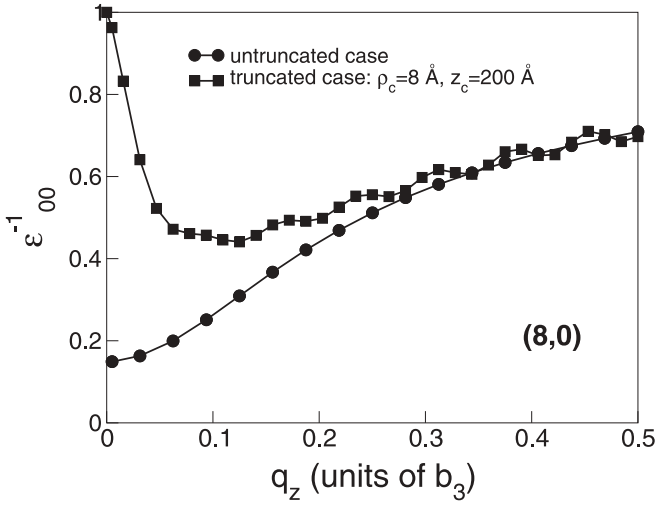

FIGURE 1 Head element of the inverse dielectric matrix $\varepsilon^{-1}_{00}(0, 0, q_z)$ for the semiconducting tube (8, 0)

Figure 2 shows the head element ε^{-1}_{00} of the static inverse dielectric matrix as a function of q_z for the metallic tube (3, 3). From its behavior at $q_z \to 0$ we can extract a Thomas–Fermi screening length of ~ 3.2 Å. Similarly we found a screening length of ~ 2.8 Å for the metallic tube (5, 0). Since in metallic tubes the Coulomb potential is effectively cut off by the dielectric matrix, there is no need to further truncate it using the procedure above.

3 Results and comparison with experiment

3.1 *Quasiparticle (single-particle) excitations*

Due to the relatively short screening length in the metallic tubes and to the fact that carbon nanotubes locally resemble a graphite sheet, we expect for the metallic tubes

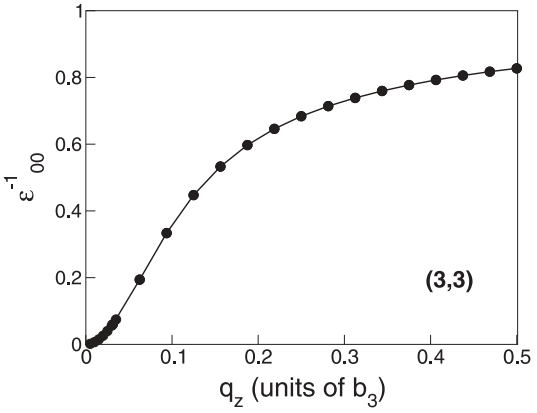

FIGURE 2 Head element of the inverse dielectric matrix $\varepsilon^{-1}_{00}(0, 0, q_z)$ for the metallic tube (3, 3)

that the *GW* quasiparticle corrections to the LDA Kohn–Sham energies be similar to those in graphite, namely a $\sim 15\%$ stretching of the LDA eigenvalues away from the Fermi level (E_F) [14]. Figure 3 shows that, for the metallic tubes (3, 3) and (5, 0), this is indeed the case.

The situation is however very different for the small-diameter semiconductor carbon nanotubes. For the semiconducting (8, 0) tube, the calculated LDA minimum band gap

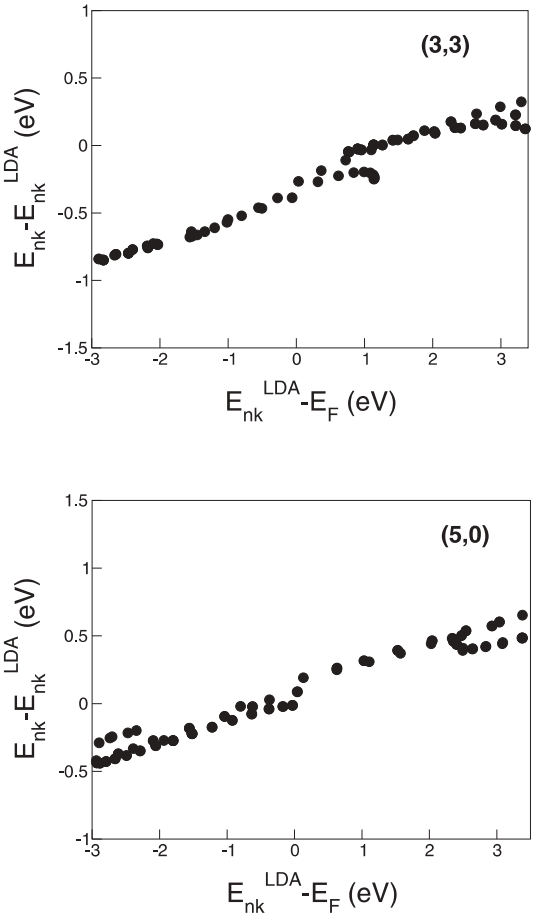

FIGURE 3 Difference between the quasiparticle energy (calculated with the *GW* approximation) and the LDA Kohn–Sham eigenvalue plotted as a function of the energy of the states for the metallic tubes (3, 3) and (5, 0)

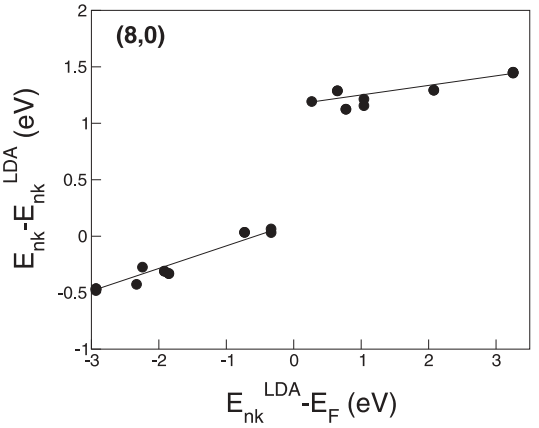

FIGURE 4 Difference between the quasiparticle energy (calculated with the *GW* approximation) and the LDA Kohn–Sham eigenvalue plotted as a function of the energy of the states for the semiconducting tube (8, 0)

is direct and only 0.60 eV at the Γ-point. Figure 4 shows that quasiparticle corrections dramatically open this gap to 1.75 eV: a 'scissor shift' of ≈ 1.15 eV is needed to obtain an accurate quasiparticle excitation spectrum near Γ. This correction is significantly larger than in bulk semiconductors with similar LDA gaps: we attribute this to the absence of metallic screening and the 1D nature of the SWCNTs which enhances the Coulomb effects (as shown also in model calculations [4]).

By applying the *GW* corrections to the LDA eigenvalues, we obtain the quasiparticle band structures, shown in Fig. 5, for the three nanotubes studied. The arrows indicate optically allowed low-energy transitions which contribute to the formation of prominent peaks in the absorption spectra, as we will see below.

3.2 *Polarization effect*

Before discussing the calculated optical spectra, we shall mention the importance of the 'depolarization effect' [15] in nanotubes for electric fields $\boldsymbol{E}$ perpendicular to $\hat{z}$. Due to the presence of bound surface charge, the polarizability for fields perpendicular to $\hat{z}$ is considerably smaller than that for fields parallel to $\hat{z}$. The physical reason for this difference is illustrated in Fig. 6 by considering the nanotube as a classical polarizable cylinder with polarizability χ (where $\boldsymbol{P} = \chi \boldsymbol{E}_{\rm tot}$) and computing the polarization induced in the tube as a function of an external electric field. In the transverse $\boldsymbol{E}$-field geometry, a dramatic reduction in the absorption spectrum results from a reduction of the polarization by the denominator $1 + 2\pi\chi$. Thus strong optical response in nanotubes is observed only for light polarized along $\hat{z}$, and we consider only this polarization below.

3.3 *Optical spectra: metallic tubes*

We first concentrate on the metallic (3, 3) tube. Figure 7 shows the quasiparticle density of states (DOS) for the (3, 3) tube, featuring a number of prominent one-dimensional (1D) van Hove singularities (vHs) near E_F. Unlike predictions from simple tight-binding models [16], these vHs are asymmetric about E_F due to strong curvature effects. The arrow in the figure indicates optically allowed low-energy

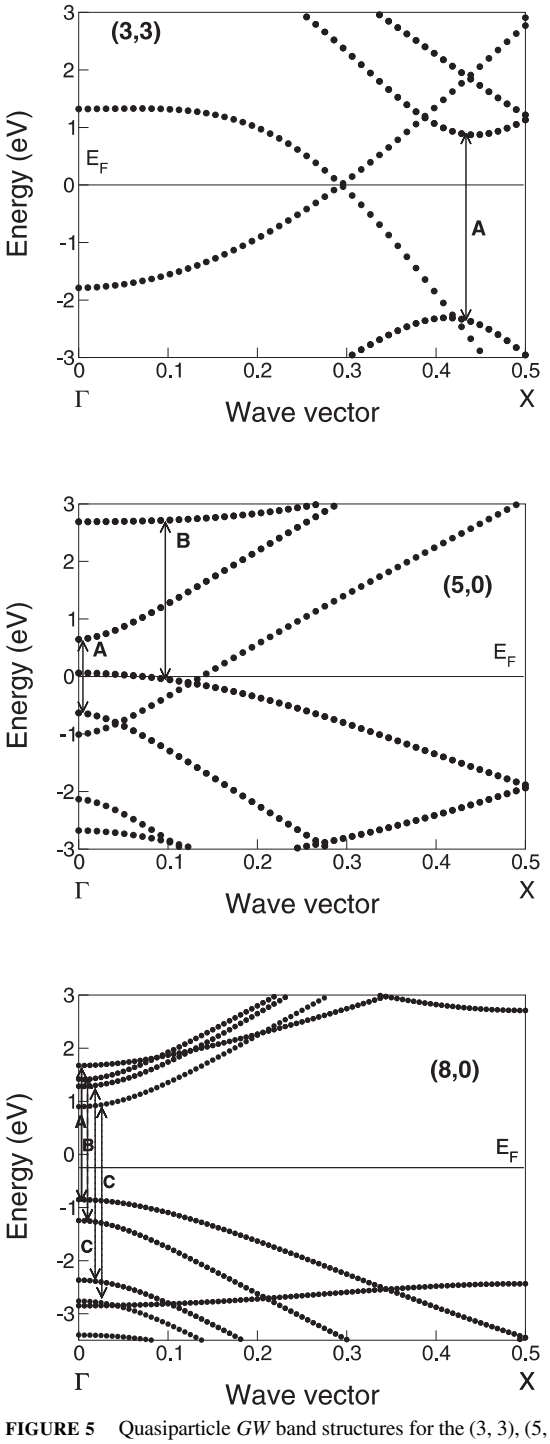

FIGURE 5 Quasiparticle *GW* band structures for the (3, 3), (5, 0) and (8, 0) tubes

transitions. For (n, n) metallic tubes, the bands forming the first vHs below E_F and the second vHs above E_F meet at the Fermi level, but optical transitions between these bands are symmetry-forbidden. The imaginary part of the dielectric function of the (3, 3) tube is shown in Fig. 8, calculated with and without electron–hole interaction. In the spectrum of the non-interacting case, a symmetry gap is clearly seen, i.e. no allowed transitions for photon energies below the peak at $\omega = 3.25$ eV. Such a gap is possible for a one-dimensional system where all $\boldsymbol{k}$-states have well-defined sym-

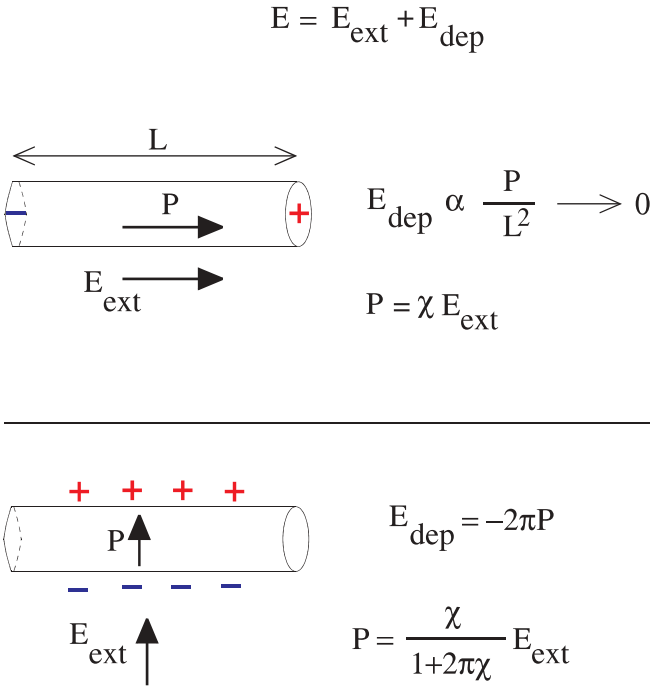

FIGURE 6 Illustration of depolarization effect. Polarizability for applied electric field parallel (*upper*) and perpendicular (*lower*) to the tube axis

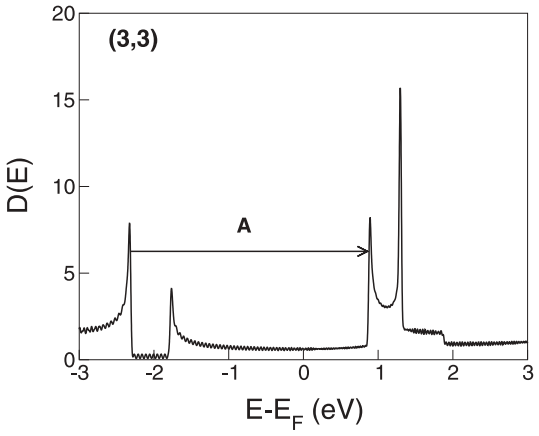

FIGURE 7 Quasiparticle density of states of the (3, 3) SWCNT

metry. Upon inclusion of the electron–hole interaction (by solving the Bethe–Salpeter equation), a single bound exciton appears in the spectrum. Though metals do not traditionally possess bound excitons, its presence here is simply a result of the symmetry gap. The fact that we see only one bound exciton is a result of the metallic screening. In particular, the effective electron–hole interaction along $\hat{z}$ resembles a $\delta(z)$ function. In 1D, the Hamiltonian

$$H = -\frac{1}{2m^*}\frac{\mathrm{d}^2}{\mathrm{d}z^2} - |V_0|\delta(z) \tag{7}$$

produces a single bound eigenstate. We find the binding energy of the A' exciton in Fig. 8 to be 86 meV.

Figure 9 shows the electron–hole probability distribution $|\Phi(\boldsymbol{r}_\mathrm{e}, \boldsymbol{r}_\mathrm{h})|^2$ for the A' bound exciton of the (3, 3) tube obtained by fixing the position of the hole $\boldsymbol{r}_\mathrm{h}$ (the green star in the figure) on a carbon π orbital. $|\Phi(\boldsymbol{r}_\mathrm{e}, \boldsymbol{r}_\mathrm{h})|^2$ describes how the quasielectron and quasihole in the photoexcited state are cor-

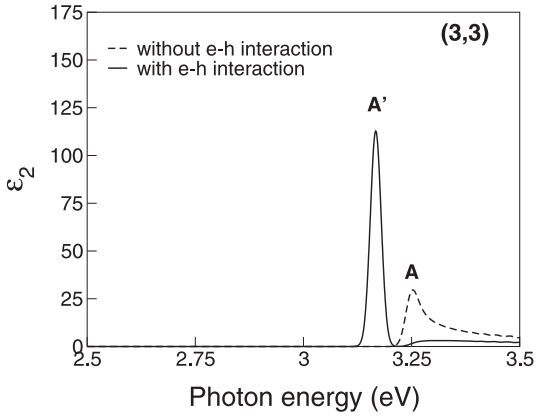

FIGURE 8 Calculated absorption spectra of the (3, 3) SWCNT. Spectra are broadened with a Gaussian factor of 0.0125 eV

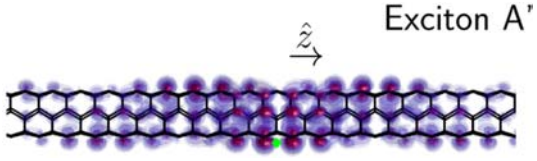

FIGURE 9 A' exciton of (3, 3) SWCNT in Fig. 8. The isosurfaces give the probability distribution $|\Phi|^2$ for finding the electron given that the hole (*green star*) is fixed on top of a carbon atom

related in real space. Figure 10 shows a more quantitative view of the extent of the bound A' exciton: $|\Phi|^2$ is plotted along $\hat{z}$ after integrating out the electron coordinates in the perpendicular plane. We see that the bound exciton A' has an extent of ~ 50 Å along $\hat{z}$. In Fig. 11 we plot the weight $\sum_{v,c} |A^S_{vck_z}|^2$ of the different electron–hole pair configurations in the bound exciton A' as a function of their momentum k_z. We see that the exciton is well localized in momentum space as well.

From the interband joint density of states (which is equal to the density of electron–hole states) shown in Fig. 12 and the position of the exciton A' in the absorption spectrum shown in Fig. 8, we can see that, given the metallic nature of the tube, the A' exciton is embedded in an electron–hole excitation continuum (which is optically forbidden) through which it can decay via various perturbations (e.g. the electron–phonon interaction).

Next we consider the metallic (5, 0) tube. Figure 13 shows the quasiparticle DOS for the (5, 0) tube. According to the band-folding scheme [16, 17], this tube should be semiconducting. However, curvature effects lead to strong $\sigma - \pi$ hybridization, forcing a band to cross E_F from above and causing another band to cross E_F from below. The latter band gives rise to the first vHs above E_F (labeled X in the figure) with its tail extending below E_F. Arrows in the figure indicate optically allowed transitions that give rise to the two peaks, labeled A and B, in the optical spectrum in Fig. 14. When neglecting electron–hole interactions, peak B has a lower intensity than A because the transitions contributing to B do not originate from the vHs X itself but from its tail. Here, however, electron–hole interactions do not create bound excitons: while the (5, 0) screening length is similar to that of the (3, 3) tube, the symmetry of the bands in the (5, 0) tube diminishes the attractive interaction term between the excited electron and hole of peaks A and B. Thus the electron–hole interaction is governed by the repulsive exchange term. This effect, again, is peculiar to nanotubes: in traditional semiconductors, the attractive direct term dominates over the exchange term. Moreover, while the strength of the exchange term is similar for peaks A and B, this is not true for the interband energy term: from the non-interacting absorption spectrum and the DOS, we can deduce that the interband energy term for peak A is larger than for peak B. As a consequence, when electron–hole interactions are included, the exchange term has a larger effect on peak B and greatly suppresses it.

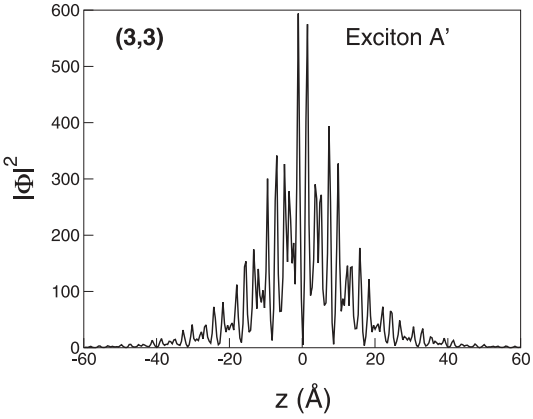

FIGURE 10 Wavefunction of the A′ exciton of the (3, 3) SWCNT. $|\Phi|^2$ from Fig. 9 is plotted after integrating out coordinates perpendicular to the tube axis

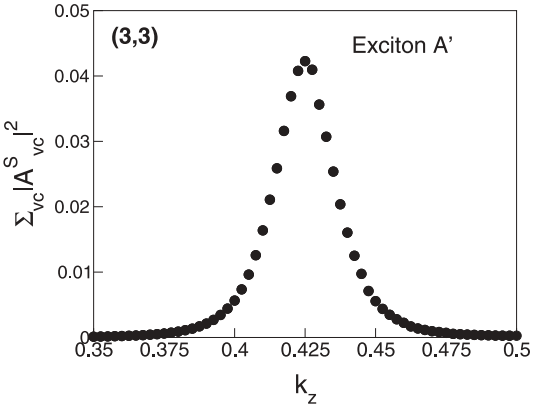

FIGURE 11 Weight of various electron–hole pair configurations contributing to the A' exciton of the (3, 3) SWCNT as a function of k_z

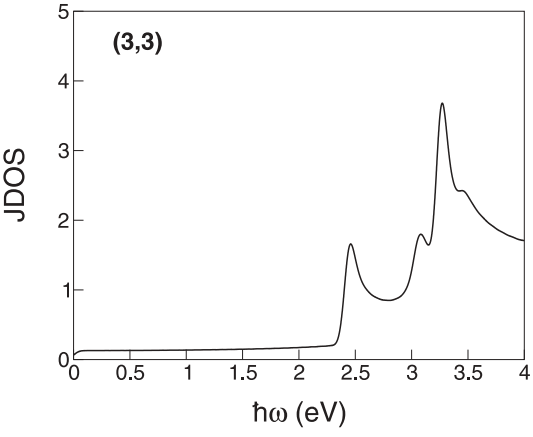

FIGURE 12 Joint quasiparticle density of states for the (3, 3) SWCNT

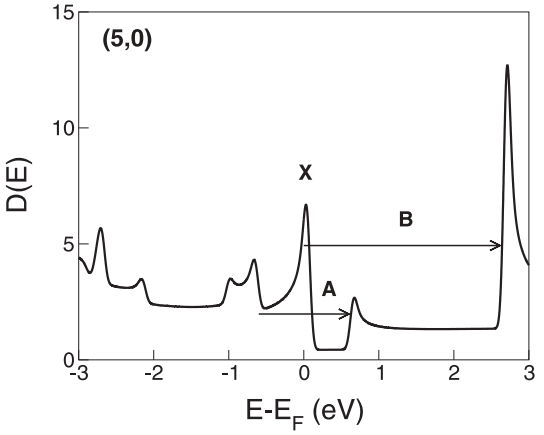

FIGURE 13 Quasiparticle density of states of the (5, 0) SWCNT

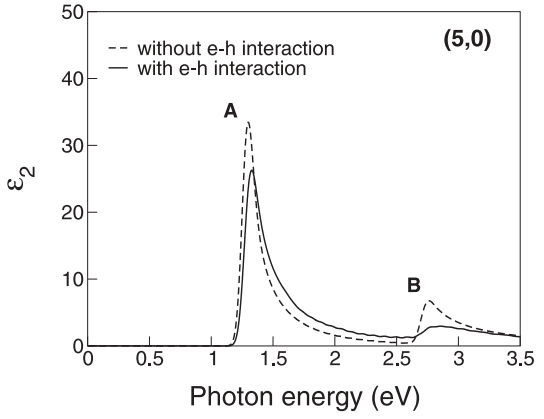

FIGURE 14 Calculated absorption spectra of the (5, 0) SWCNT

For the metallic tubes (3, 3) and (5, 0) there are relevant experiments for us to directly compare our results to. In the work of Li et al. [1], small-diameter SWCNTs were grown inside zeolite channels of $AlPO_4$. The absorption spectra of these samples were measured, and three prominent peaks were found (see Table 1). The diameter of the tubes was determined to be 4 Å, and there are three possible chiralities compatible with this diameter: (3, 3), (5, 0) and (4, 2). However, experimentally it was not possible to decide which tube contributes to which prominent peak. To better reproduce the experimental conditions, we carried out calculations for the (3, 3) and (5, 0) tubes in the presence of a dielectric background of $AlPO_4$. The dielectric background is accounted for by adding a model dielectric function [18] for $AlPO_4$ to the dielectric matrix of the metallic SWCNTs considered. Because the electron–hole attraction involves very small momenta transfer in the screened Coulomb interaction (see Fig. 11) and since for very small momentum the dielectric matrix of metallic tubes is much larger than the background dielectric constant of $AlPO_4$, the influence of the background $AlPO_4$ on the optical spectra of these tubes is actually negligible. Table 1 shows that our results for the metallic tubes (3, 3) and (5, 0) are in very good quantitative agreement with experiment and provide a definitive identification for two of the observed peaks. We conclude that the remaining peak at 2.1 eV is due to the (4, 2) tube (other calculations [19, 20] performed at the RPA level – without including electron–hole interactions – as well as a recent TDLDA (time-dependent local density approximation) calculation [21] lead to the same conclusion [22]). Moreover, the many-electron suppression of peak B in the (5, 0) spectrum explains the absence of any observed feature in the experimental spectra at ≈ 2.8 eV.

Nanotube	Theory	Experiment*
(5, 0)	1.33 eV	1.37 eV
(3, 3)	3.17 eV	3.1 eV
(4, 2)	–	2.1 eV

* [1]

TABLE 1 Peak positions and optical transitions in 4 Å SWCNTs

3.4 *Optical spectra: semiconducting tubes*

Figure 15 shows the quasiparticle DOS of the (8, 0) SWCNT. The arrows indicate optically allowed transitions which form three distinct low-energy peaks (labeled A, B, C) in the non-interacting absorption spectrum in Fig. 16. When electron–hole interactions are included, we find far more dramatic excitonic effects than in the metallic cases: each peak in the non-interacting case gives rise to a series of visible exciton lines with large binding energies. The binding energies are 0.99 eV, 0.86 eV and 1.00 eV for the lowest-energy excitons A'_1, B'_1 and C'_1 respectively. These binding energies are more

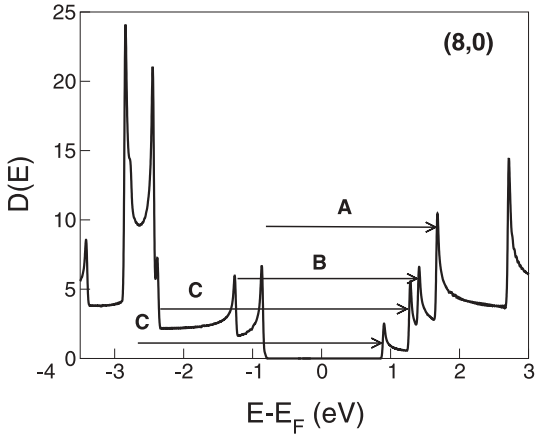

FIGURE 15 Quasiparticle density of states of the (8, 0) SWCNT

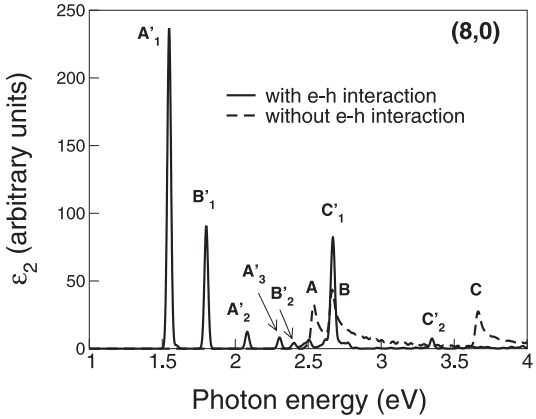

FIGURE 16 Calculated absorption spectra of the (8, 0) SWCNT. Spectra are broadened with a Gaussian factor of 0.0125 eV

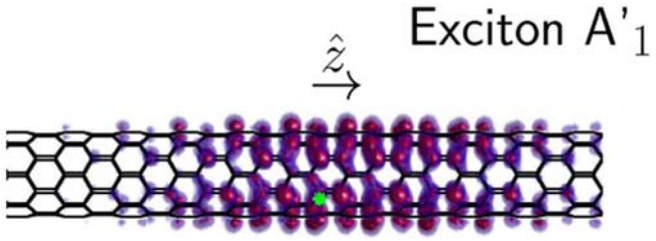

FIGURE 17 Similar plot as in Fig. 9 for the A_1' exciton of the (8, 0) SWCNT

than 10 times larger than those in bulk semiconductors with similar gaps, and the excitonic effects qualitatively change the profile of the spectrum. Again, these effects stem from the long-range nature of the screened Coulomb interaction and the 1D nature of the SWCNTs: e.g. the binding energy of a 1D hydrogenic system is infinite due to the long-range Coulomb interaction [23]. We also note that the electron–hole interaction reverses the relative intensity of the first and second prominent optical peaks.

Our calculation predicts that there are two varieties of strong excitons in the (8, 0) tube: bound excitons with energies below the non-interacting optical gap (the A' and B' series) and resonant excitons with energies above the non-interacting optical gap (the C' series). Figure 17 shows the real-space, electron–hole pair probability distribution for the A_1' bound exciton of the (8, 0) tube (again, the hole position is fixed on top of a π orbital; due to the inequivalency of adjacent carbon atoms, the electron distribution is not completely symmetric about this particular hole position). Figure 18 shows the degree of localization along $\hat{z}$ of the bound A_1', A_2', B_1' and the resonant C_1' exciton. The extent of the 'ground-state' excitons A_1', B_1' and C_1' is ~ 25 Å, while for the 'excited-state' visible excitons (such as A_2'), the extent is larger. The delocalized part of the resonant exciton C_1' has an envelope function with period $2\pi/|k_z|$, where k_z is the momentum of the uncorrelated electron–hole pairs forming the delocalized part.

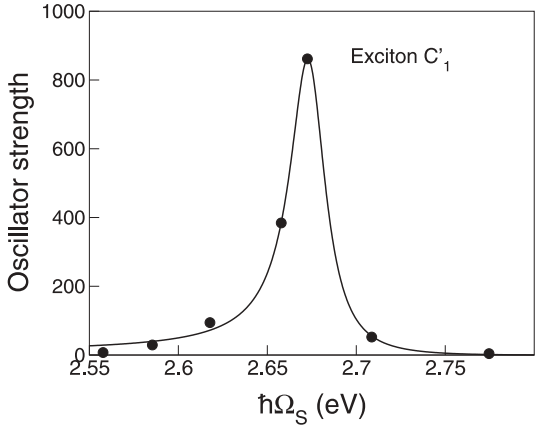

FIGURE 19 Fano profile for the resonant exciton C_1' of the (8, 0) SWCNT. The *dots* are the calculated oscillator strength and the *solid curve* is a fit to a Fano profile

The oscillator strength for the C_1' exciton can be fitted nicely by a Fano profile [24], see Fig. 19. From its width we extract a resonant lifetime $\tau_{\rm res} \approx 50$ fs.

Our results for the (8, 0) tube agree well with the experimental results of Bachilo et al. [3, 25]. In their work, spectrofluorimetric measurements on various semiconducting SWCNTs with diameters ranging from 0.62 to 1.31 nm and chiral angle from 3 to 28 degrees were performed. From their analysis, they were able to assign optical transitions to spe-

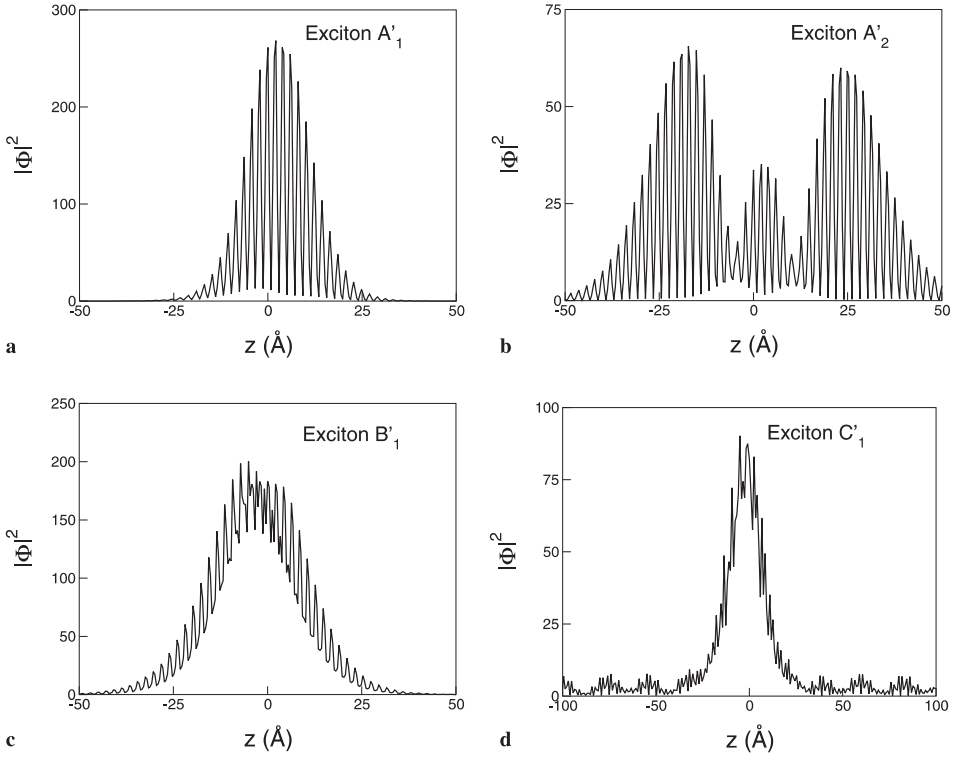

FIGURE 18 Similar plot as in Fig. 10 for the A_1', A_2', B_1' and C_1' excitons of the (8, 0) SWCNT

Transition	Theory	Experiment*
ν_{11}	1.55 eV	1.60 eV
ν_{22}	1.80 eV	1.88 eV
ν_{22}/ν_{11}	1.16	1.17

* Obtained from experimental fits of [3, 25]

TABLE 2 Lowest two optical transition energies of the (8, 0) SWCNT

cific (n, m) nanotubes. Though the (8, 0) tube was not present in their SWNT samples, they provided fits for the first and second optical transition energies (ν_{11} and ν_{22}) for tubes of similar size, and presented expressions for transition energies as a function of tube diameter and chiral angle. These fits were shown to work well for a wide range of (n, m) values [3, 25]. For the (8, 0) tube, their fits yield a ratio $\nu_{22}/\nu_{11} = 1.17$. The traditional π-electron tight-binding model in the non-interacting framework predicts a ratio of 2, and the deviation of the experimental ratio from 2 has been puzzling [26–28]. However, as shown in Table 2, our results for the main peaks in the spectrum of the (8, 0) tube (peaks A_1' and B_1') produce a ratio which is in excellent agreement with that predicted from the fit to experiment. The deviation of ν_{22}/ν_{11} from 2 is a consequence of both 'effective' one-electron (i.e. quasiparticle band structure) and many-electron (here, electron–hole interaction) effects: one needs to include both effects for a proper quantitative understanding.

4 Conclusion

In conclusion, we have studied the optical absorption spectra of metallic and semiconducting small-diameter SWCNTs. Quasiparticle effects were included by computing self-energy corrections to density-functional theory Kohn–Sham band energies within the *GW* approximation. Excitonic effects on the optical spectra were computed with the Bethe–Salpeter equation. The calculated optical spectra are in excellent agreement with available experimental data. We show that electron–hole interactions (which can be either attractive or repulsive) play a crucial role, especially in the case of semiconducting tubes, in explaining experimental results. Large excitonic features for both semiconducting and metallic tubes are seen to be due to the quasi-1D nature of SWCNTs, and the manner in which they affect the spectra depends on the rotational symmetries of the tubes.

ACKNOWLEDGEMENTS This work was supported by the NSF under Grant No. DMR0087088 and the Office of Energy Research, Office of Basic Energy Sciences, Materials Sciences Division of the US Department of Energy (DOE) under Contract No. DE-AC03-76SF00098. Computer time was provided by the NSF at the National Center for Supercomputing Applications and by the DOE at the Lawrence Berkeley National Laboratory (LBNL)'s NERSC center. Portions of this work were performed under the auspices of the DOE by the University of California Lawrence Livermore National Laboratory (LLNL) under Contract No. W-7405-Eng-48. Collaborations between LLNL and LBNL were facilitated by the DOE's Computational Materials Sciences Network.

REFERENCES

1 Z.M. Li, Z.K. Tang, H.J. Liu, N. Wang, C.T. Chan, R. Saito, S. Okada, G.D. Li, J.S. Chen, N. Nagasawa, S. Tsuda: Phys. Rev. Lett. **87**, 127 401 (2001)
2 M.J. O'Connell, S.M. Bachilo, C.B. Huffman, V.C. Moore, M.S. Strano, E.H. Haroz, K.L. Rialon, P.J. Boul, W.H. Noon, C. Kittrell, J. Ma, R.H. Hauge, R.B. Weisman, R.E. Smalley: Science **297**, 593 (2002)
3 S.M. Bachilo, M.S. Strano, C. Kittrell, R.H. Hauge, R.E. Smalley, R.B. Weisman: Science **298**, 2361 (2002)
4 T. Ando: J. Phys. Soc. Jpn. **66**, 1066 (1996)
5 J.A. Misewich, R. Martel, Ph. Avouris, J.C. Tsang, S. Heinze, J. Tersoff: Science **300**, 783 (2003)
6 M. Rohlfing, S.G. Louie: Phys. Rev. B **62**, 4927 (2000)
7 W. Kohn, L.J. Sham: Phys. Rev. **140**, A1133 (1965)
8 M.S. Hybertsen, S.G. Louie: Phys. Rev. B **34**, 5390 (1986)
9 L. Hedin: Phys. Rev. **139**, A796 (1965)
10 G. Strinati: Phys. Rev. B **29**, 5718 (1984)
11 N. Troullier, J.L. Martins: Phys. Rev. **43**, 1993 (1991)
12 L. Kleinman, D.M. Bylander: Phys. Rev. Lett. **48**, 1425 (1982)
13 X. Blase, L.X. Benedict, E.L. Shirley, S.G. Louie: Phys. Rev. Lett. **72** 1878 (1994)
14 S.G. Louie: in *Topics in Computational Materials Science*, ed. by C.Y. Fong (World Scientific, Singapore 1997) p. 96
15 H. Ajiki, T. Ando: Physica B **201**, 349 (1994)
16 R. Saito, M. Fujita, G. Dresselhaus, M.S. Dresselhaus: Appl. Phys. Lett. **60**, 2204 (1992)
17 N. Hamada, S.I. Sawada, A. Oshiyama: Phys. Rev. Lett. **68**, 1579 (1992)
18 Z.H. Levine, S.G. Louie: Phys. Rev. B **25**, 6310 (1982)
19 H.J. Liu, C.T. Chan: Phys. Rev. B **66**, 115 416 (2002)
20 M. Machon, S. Reich, C. Thomsen, D. Sanchez-Portal, P. Ordejon: Phys. Rev. B **66**, 155 410 (2002)
21 A.G. Marinopoulos, L. Reining, A. Rubio, N. Vast: Phys. Rev. Lett. **91**, 046 402 (2003)
22 The calculation for the (8, 0) tube (with 32 atoms in the unit cell) was already very challenging on modern supercomputers. We are currently studying the (4, 2) tube, which has 56 atoms in the unit cell, but this is a far more difficult calculation (our calculations scale as the number of atoms to the fourth power)
23 R. Loudon: Am. J. Phys. **27**, 649 (1959)
24 U. Fano: Phys. Rev. **124**, 1866 (1961)
25 R.B. Weisman, S.M. Bachilo: Nano Lett. **3**, 1235 (2003)
26 M. Ichida, S. Mizuno, Y. Tani, Y. Saito, A. Nakamura: J. Phys. Soc. Jpn. **68**, 3131 (1999)
27 X. Liu, T. Pichler, M. Knupfer, M.S. Golden, J. Fink, H. Kataura, Y. Achiba: Phys. Rev. B **66**, 045 411 (2002)
28 C.L. Kane, E.J. Mele: Phys. Rev. Lett. **90**, 207 401 (2003)